Honing the accuracy of extreme ultraviolet optical system testing: at-wavelength and visible-light measurements of the ETS Set-2 projection optic

Kenneth A. Goldberg*[a], Patrick Naulleau[a], Jeffrey Bokor[a,b], and Henry N. Chapman[c]
[a]Center for X-Ray Optics, Lawrence Berkeley National Laboratory, Berkeley, CA 94720
[b]EECS Department, University of California, Berkeley, CA 94720
[c]Lawrence Livermore National Laboratory, L-395, Livermore, CA 94550

ABSTRACT

As the quality of optical systems for extreme ultraviolet lithography improves, high-accuracy wavefront metrology for alignment and qualification becomes ever more important. To enable the development of diffraction-limited EUV projection optics, visible-light and EUV interferometries must work in close collaboration. We present a detailed comparison of EUV and visible-light wavefront measurements performed across the field of view of a lithographic-quality EUV projection optical system designed for use in the Engineering Test Stand developed by the Virtual National Laboratory and the EUV Limited Liability Company. The comparisons reveal that the present level of RMS agreement lies in the 0.3-0.4-nm range. Astigmatism is the most significant aberration component for the alignment of this optical system; it is also the dominant term in the discrepancy, and the aberration with the highest measurement uncertainty. With EUV optical systems requiring total wavefront quality in the $\lambda_{EUV}/50$ (0.25 nm) range, and even higher surface-figure quality for the individual mirror elements, improved accuracy through future comparisons, and additional studies, are required.

Keywords: interferometry, extreme ultraviolet lithography, EUV, at-wavelength testing, EUV visible-light comparison.

1. INTRODUCTION

Diffraction-limited optical systems designed for extreme ultraviolet (EUV) lithography operate with 13-nm-wavelength light and have total system wavefront error tolerances in the $\lambda_{EUV}/50$ (25 nm) range, for the low-spatial-frequency, or *figure* aberrations. Multiple multilayer-coated reflective optical elements are combined to form a single compound projection lens for EUV lithography. To date, the designs of these systems have included two-element small-field-of-view optics for research purposes and larger, 3, 4, and 6-element optical systems with wide, arc-shaped ring-fields of view. For every reflective EUV optic, the combined system wavefront at each point in the field depends on the surface profile and alignment of each mirror, and on the spatially varying multilayer-coating properties.

Two interferometers have been constructed to measure the system wavefront and perform fine alignment of the projection optics designed for the Engineering Test Stand (ETS)[1] which is now operational at Sandia National Laboratories. Two four-mirror ring-field optical systems, referred to as the ETS Set-1 and Set-2 optics, have been fabricated for the ETS. The interferometers are a visible-light phase-shifting diffraction interferometer (PSDI)[2] at Lawrence Livermore National Laboratory (LLNL), and an EUV phase-shifting point diffraction interferometer (PS/PDI)[3] at Lawrence Berkeley National Laboratory (LBNL). Both interferometers, which have been described previously, operate on the principle of point diffraction to produce spherical reference wavefronts, and both are capable of measuring the system wavefront at arbitrary positions across the entire ring-field of view.

Recently EUV interferometry performed with the phase-shifting point diffraction interferometer (PS/PDI), developed at Lawrence Berkeley National Laboratory (LBNL), has demonstrated RMS surface-figure-measuring accuracy levels in the sub-$\lambda_{EUV}/200$, 0.06-nm range within a 0.1 numerical aperture. These results were achieved, and verified by *in situ* null tests performed during the measurement of several diffraction-limited EUV optical systems. The accuracy of the visible-light interferometer is inferred by comparison with EUV wavefront measurements made on the same optical system.

*Correspondence: Email: KAGoldberg@lbl.gov; Telephone: 510-495-2261; Fax: 510-486-4550

In this paper, we describe the comparison of visible-light and EUV wavefront measurements of the ETS Set-2 optic. The measurement of the Set-1 optic was performed in 1999–2000 and has been reported previously.[4]

In our tests, the average level of RMS surface-figure agreement between the EUV PS/PDI and the visible-light PSDI is 0.35 ± 0.11 nm. For this off-axis reflective optical system, astigmatism is the dominant aberration term used in the alignment process. Astigmatism has also been the most challenging aberration to measure accurately: it comprises the majority of the wavefront discrepancy at this time. For $\lambda_{EUV}/50$-quality EUV optical systems, the total wavefront errors must be in the 0.25-nm range; interferometers suitable for testing these optics must have an accuracy at least several times higher, beyond a level that is available today. The importance of continued improvement and ongoing research is clear.

In practice, the agreement between visible-light and EUV measurements of the same EUV optical system relies on nearly ideal conditions. Whereas the phase of the EUV reflected light depends sensitively on the thickness profile of the multilayer coatings, visible-light reflection is almost insensitive to the multilayer profile. Furthermore, the presence of carbon contamination on a mirror's surface can create a significant difference between the measured visible-light and EUV reflected phase (and amplitude).[5] While the former concerns have been significantly allayed by recent improvements in the accuracy and repeatability of multilayer-deposition techniques,[6] carbon contamination has the potential to compromise visible-light measurements made on systems that have been exposed to EUV light and have suffered carbon deposition on the mirror surfaces.

2. TWO INTERFEROMETERS

The EUV PS/PDI and visible-light PDSI interferometers were constructed to evaluate the system wavefront at arbitrary positions across the field of view. Both interferometers can also measure distortion (image placement error) across the field; yet, currently only the visible-light interferometer has been calibrated to do so. Measurements of the field-dependent optical performance, across the large ring-field imaging area, provide feedback for the alignment of the individual mirror elements, enabling optimal imaging quality to be achieved. Detailed descriptions of the PS/PDI[3,4] and the PSDI[2,7] have been published previously, and the measurement of the ETS Set-1 optical system (an optic of identical design to the ETS Set-2 optic, but with lower wavefront quality) has been reported.[8] In addition, the iterative alignment algorithm, designed to optimize lithographic performance across the optic's entire field of view, has also been published. The scope of this paper is limited to the wavefront measurements made by these two interferometers.

The EUV interferometer's light source is an undulator beamline at the Advance Light Source synchrotron radiation facility in Berkeley, California.[9] The source is tunable with a bandwidth, $\lambda/\Delta\lambda$, of approximately 200. Based on the measured peak transmission wavelength of the ETS Set-2 optic, the interferometer was operated at 13.35-nm wavelength. The visible-light interferometer's light source is a Spectra Physics short coherence length frequency-doubled YAG operating at a wavelength of 532.2 nm with a longitudinal coherence length of approximately 5 mm.

The two interferometers operate at the same design temperature of 21ºC, and both interferometers are constructed within temperature-controlled environments to guarantee temperature stability better than 0.1°C during the measurements. The visible-light and EUV measurements required approximately 4 and 6 hours to complete, respectively.

Between the visible-light and EUV measurements, the ETS Set-2 optic was transported by truck in a specially-designed shipping container from LLNL to LBNL, a distance of approximately 45 miles (74 km). During shipping and a two-week period of initial inspection with EUV light, the optic was allowed to reach the ambient temperature, approximately 23°C.

Both interferometers are capable of measuring the wavefront at arbitrary positions within the field of view. Forty-five predefined field positions, arranged into nine columns of five points, are specified by the alignment algorithm.[2] Both interferometers utilize their own lithographically-fabricated arrays of pinholes to define the field point measurement positions. A substantial effort was made to guarantee that the field-point positions, and with them their conjugate positions, in the EUV and visible-light interferometers were closely matched. The ETS Set-2 optic housing is constructed with a *metrology tower* containing three capacitance micrometers for height and tilt sensing, and two miniature, in-vacuum microscope cameras for lateral positions sensing.[10] Both the visible-light and EUV interferometry object-side pinhole arrays are fabricated onto monolithic substrates using lithography techniques that allow the individual pinholes to be placed to submicron accuracy with respect to fiducials on the masks. These fiducials are used in conjunction with the microscope

cameras on the metrology tower to position the pinhole arrays in known locations relative to the optic under test. The lateral positioning accuracy is approximately 10 microns, well within the alignment tolerance of 100 microns set by the alignment algorithm.

3. WAVEFRONT MEASUREMENTS

The primary goal of this comparison is to reach an objective evaluation of the level of agreement between these two interferometers, considering their respective measurements as separate and independent.

The interferometric wavefront measurements serve to both evaluate the wavefront performance and to improve it through alignment. For the purposes of alignment, and throughout this paper, the measured wavefront quality is based solely on the low-spatial-frequency surface-figure aberrations, as determined by the first-37 Zernike polynomial terms: here, the ordering of the polynomials follows the *FRINGE* Zernike convention.[11] Restricting the analysis to the surface-figure aberrations, the RMS wavefront error magnitudes quoted are based on the first-37 Zernike polynomial terms alone. Tilt and defocus aberrations are currently only meaningful in the visible-light interferometer where the three-dimensional coordinates of the pinholes are accurately known. Although these aberrations are required for system alignment, they, along with piston, are excluded from the wavefront analysis.

Visible-light wavefront measurements at each field point include the average of six 32-iteration phase-shifting series, where each series uses seven to nine phase steps. The EUV wavefront measurements use a single phase-shifting series with five steps at each field position.

For each wavefront measurement, a 37-term Zernike polynomial fit is performed on the raw wavefront data to determine the surface figure (low spatial-frequency only). The interferogram analysis and wavefront fitting procedures have been described previously.[4] The fit coefficients of the individual Zernike polynomials are reported using the RMS convention: here a coefficient magnitude of 1 nm represents a 1-nm RMS contribution from a given aberration term.

Owing to the non-normal angle of incidence of the beam onto the pupil's aperture (situated on the circular, on-axis, third mirror element), the wavefront subtends a slightly elliptical domain with 0.9% eccentricity. The EUV and visible-light wavefronts are evaluated using an intermediate set of aberration polynomials that are orthogonal on the measurement domain. In both interferometers, the analysis is complicated by the motion and rotation of the projected pupil onto the stationary CCD cameras.

3.1 Comparison

Comparisons of visible-light and EUV measurements of the same wavefront are based on the *difference wavefront*, defined as the subtractive difference of the two independent wavefront measurements, reconstructed on the same domain using the Zernike fitting coefficients. Comparisons are made at 43 of the 45 pre-defined field point positions; two points are excluded from the visible-light data because of pinhole quality concerns. Figure 1 shows the field-position numbering convention used by both groups.

Within the ETS optical system, light from the object plane reflects from each of the four component mirrors to produce the image; whence the measured system wavefront contains the additive contribution of the surface profile of each mirror. Light from separate points in the field of view follow different paths through the optical system and sample different regions of the mirror surfaces as they propagate. In this way, the individual hills and valleys of each mirror surface appear in different locations within the measured pupil. When separate wavefronts are compared, slight discrepancies in their field-positions of measurement will appear as displacements in the fine features of the wavefront. For this reason, the difference wavefronts will contain some shear from these features, the magnitude of which is dependent on the conjugate position discrepancy between the two measurements. Fortunately, these shear effects do not contribute significantly to the

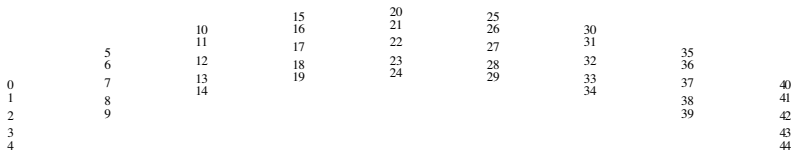

Fig. 1. Field point numbering convention used to identify 45 wavefront-measurement points within the field. The points are arranged as shown for an observer looking up into the optic from the wafer plane. The field is 26-mm wide in the image plane and spans a 30° arc.

measurement of the low-spatial-frequency Zernike polynomials. Furthermore, the presence and consequences of these minor position discrepancies must be included in the full independent comparison of these two interferometries. Post-measurement efforts to minimize these effects in the wavefront data would compromise the objectivity of the comparison.

Figure 2 shows a side-by-side comparison of four of the 45 wavefronts measured with visible-light and EUV. The EUV data, recorded with the PS/PDI, has a lower spatial-frequency bandwidth than the visible-light data because the EUV light passes through a 3-μm-wide image plane window. The window behaves as a low-pass spatial filter but does not affect the measurement of the much-lower-frequency aberration terms of interest. The wavefront data is represented on a grayscale covering the range [–5.0, 5.0] nm. The RMS magnitudes of four aberration terms and the overall wavefront error are given below each wavefront. The amplitudes of the first-37 Zernike polynomial terms (excluding tilt and defocus) are added as the root-sum-of-squares to form the overall RMS magnitude.

The corresponding difference wavefronts are shown in the third column of Fig. 2, scaled on the range [–1.5, 1.5] nm and reconstructed from the first-37 Zernike polynomials. Each wavefront shows some residual low-spatial-frequency aberrations, such as astigmatism, coma, etc.

A comparison of the RMS aberration magnitudes of the individual measured wavefronts, and for the difference wavefronts, is shown in Fig. 3 for all of the measured field points. The aberration coefficients vary smoothly across the field of view, as shown in Fig. 3(b); the saw-tooth appearance in the plots comes from unwrapping the nine columns of points into a single vector of coefficients.

Analysis of the difference wavefront RMS magnitudes shows that the level of agreement between the two interferometers, averaged across the field, is 0.35 ± 0.11 nm (0.35 nm is approximately $\lambda_{EUV}/38$), with a median value of 0.39, and spans a range of 0.14 to 0.58 nm. A histogram of the wavefront difference RMS magnitudes is shown in Fig. 3(c).

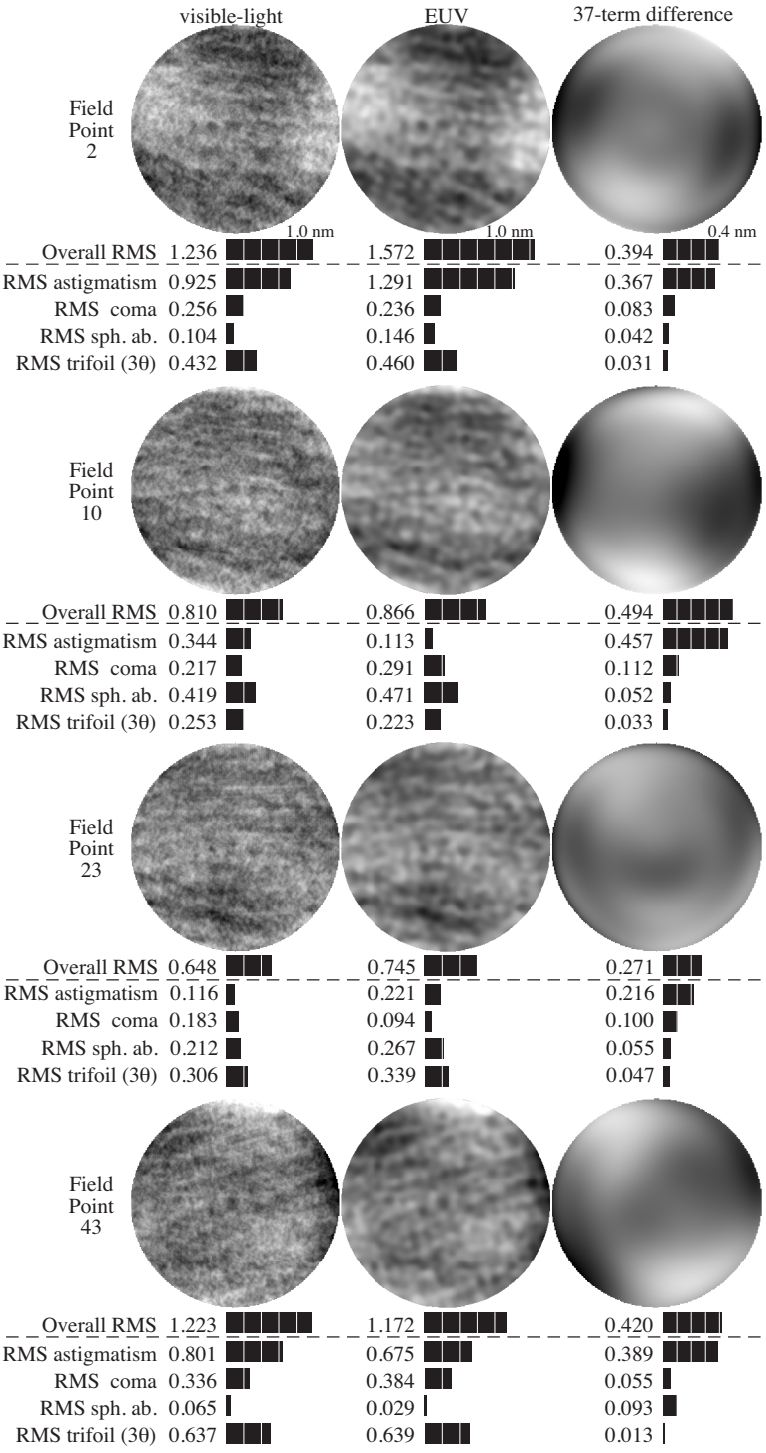

Fig. 2. Side-by-side visible-light and EUV wavefront measurements at four field points. The wavefronts are rendered on the same grayscale range [–5.0, 5.0] nm; the difference wavefronts in the third column are scaled on [–1.5, 1.5] nm. The RMS magnitudes are given for a 37-term Zernike polynomial fit and for four specific low-ordered aberrations. Astigmatism is the dominant aberration in the difference wavefronts.

The plots and contours in Fig. 4 isolate the individual aberration components that represent astigmatism, coma, trifoil, spherical aberration, and a higher-ordered spherical aberration term. The level of agreement for the individual Zernike polynomial coefficients is shown in Table 1. Here, the quantities of interest are the field-averaged *mean difference*, $\bar{\Delta}$, and its standard deviation, σ_Δ.

The majority of the discrepancy is concentrated in the low-spatial-frequency aberration terms, particularly astigmatism. For most of the Zernike terms, the field-averaged level of agreement below $\lambda_{EUV}/1000$, with larger standard deviation magnitudes in the range of 0.3 down to 0.15 nm ($\lambda_{EUV}/50$ to $\lambda_{EUV}/90$). Yet for astigmatism, the relatively large $\bar{\Delta}$ values (0.280 ± 0.149 nm for Z_4, and 0.053 ± 0.091 nm for Z_5) indicate the presence of an important systematic difference between the two interferometers. Small-field EUV imaging experiments performed after the EUV interferometry have qualitatively verified the low astigmatism predicted from the EUV interferometry, near the center of the field of view.[12]

3.2 Field position uncertainty

One challenge for the inter-comparison of wavefront measurements recorded on different interferometers is to guarantee that the field points where the measurements are performed are well matched between the different interferometers. Since the wavefront is spatially varying across the field, a discrepancy in the field positions would introduce some level of difference.

As described above, great care has been taken to ensure that the field points used in the visible-light and EUV interferometers are well matched, to the level required by the alignment algorithm and by this inter-comparison (tens of microns). If there were a significant field-point-position discrepancy, the observed wavefront difference at a point would contain a shear term related to the gradient of the changing wavefront, including contributions from each mirror surface and a parallax from the displaced measurement points. That shear would most severely impact the aberration terms with the highest spatial frequency, i.e. those with the highest local slope. The relatively high level of agreement in the higher-ordered aberration terms, compared to the lower-ordered terms, leads to the conclusion that field-position discrepancies are not contributing to the measurement discrepancy observed in the lower-ordered aberration terms.

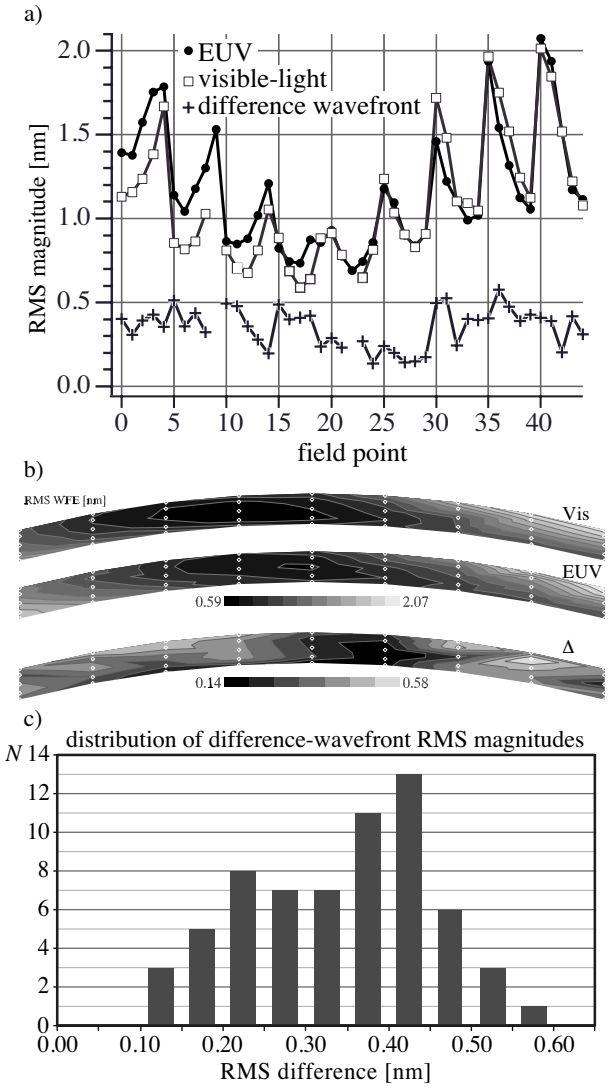

Fig. 3. (a) Wavefront surface figure RMS magnitudes at each measured field point. The level of agreement is represented by the magnitudes of the difference wavefronts, which are also shown. **(b)** The same RMS magnitude and difference magnitude data are shown in contour plots. The sawtooth appearance of the plots in (a) is a byproduct of the field point numbering convention (a linear representation of two-dimensional data)—the contour plots show that data is smoothly varying. **(c)** A histogram of difference wavefront magnitudes shows an average level of agreement of 0.35 ± 0.11 nm with a median value of 0.39 nm, spanning a range of 0.14 to 0.58 nm.

3.3 EUV measurement precision and accuracy

Figure 5 shows the field-averaged EUV measurement uncertainty in the individual Zernike polynomial coefficients, indicating the measurement precision. The uncertainty numbers are calculated by studying the individual, single-exposure wavefront measurements from a phase-shifting series that is combined to form a single wavefront measurement. Fringe analysis and wavefront fitting are performed on the individual measurements, and the standard deviation of the coefficients is calculated at each field point. The field-average of those standard deviations is what we call the uncertainty in each coefficient. Except for astigmatism, the coefficient uncertainty is consistently below the $\lambda_{EUV}/1000$ level.

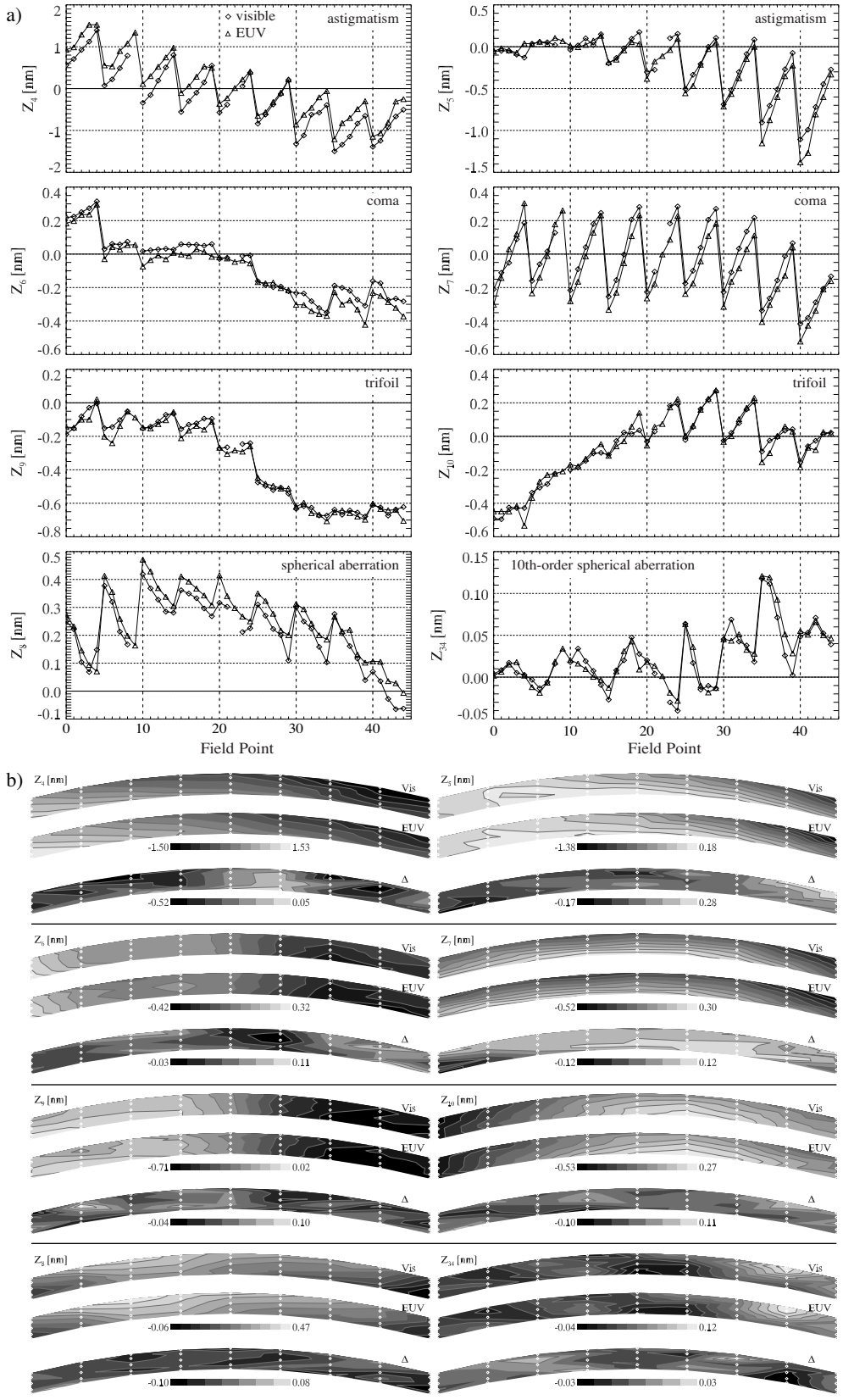

Fig. 4. Comparison of some representative Zernike polynomial coefficient values across the field of view. **(a)** EUV and visible-light coefficients are shown for eight of the 37 separate aberrations terms: including the paired astigmatism, coma, and trifoil terms, and spherical aberration, both 4th order and 10th order. In all cases, the aberration coefficients vary smoothly across the field of view: the saw-tooth appearance in the plots comes from unwrapping the nine columns of points into a single vector of coefficients. **(b)** Contour plots showing the measured behavior of the visible-light and EUV aberration coefficients, and their difference, across the field of view. This is the same data as is shown in the plots (a), above. The field-averaged difference and standard deviation of all of the measured Zernike polynomial coefficients are given in Table 1.

Table 1. The average difference or *discrepancy* between the visible-light and EUV Zernike polynomial coefficients are shown for each aberration term, excluding measurement-dependent piston, tilt, and defocus. The eight individual terms shown in Fig. 4 are indicated in the table by asterisks. Notice that the most significant difference comes from astigmatism, in particular the Z_4 term.

abb.	$\overline{\Delta} \pm \sigma_\Delta$ [nm]	abb.	$\Delta \pm \sigma_\Delta$ [nm]	abb.	$\Delta \pm \sigma_\Delta$ [nm]	abb.	$\Delta \pm \sigma_\Delta$ [nm]	abb.	$\Delta \pm \sigma_\Delta$ [nm]
* Z_4	-0.280 ± 0.149	* Z_{11}	0.047 ± 0.025	Z_{18}	0.006 ± 0.016	Z_{25}	0.009 ± 0.022	Z_{32}	0.002 ± 0.010
* Z_5	0.053 ± 0.091	Z_{12}	0.006 ± 0.019	Z_{19}	-0.003 ± 0.018	Z_{26}	0.015 ± 0.017	Z_{33}	0.008 ± 0.010
* Z_6	0.041 ± 0.032	Z_{13}	0.000 ± 0.013	Z_{20}	0.014 ± 0.015	Z_{27}	-0.007 ± 0.020	* Z_{34}	-0.002 ± 0.011
* Z_7	0.054 ± 0.050	Z_{14}	0.000 ± 0.016	Z_{21}	0.000 ± 0.017	Z_{28}	0.001 ± 0.016	Z_{35}	0.001 ± 0.015
* Z_8	-0.040 ± 0.029	Z_{15}	-0.017 ± 0.023	Z_{22}	0.002 ± 0.014	Z_{29}	-0.001 ± 0.014	Z_{36}	0.008 ± 0.011
* Z_9	0.013 ± 0.032	Z_{16}	-0.011 ± 0.035	Z_{23}	0.017 ± 0.015	Z_{30}	-0.007 ± 0.014		
* Z_{10}	-0.002 ± 0.038	Z_{17}	-0.005 ± 0.034	Z_{24}	-0.002 ± 0.024	Z_{31}	-0.006 ± 0.015		

Z_4, Z_5: astigmatism
Z_6, Z_7: coma
Z_8: spherical aberration
Z_9, Z_{10}: trifoil (3θ)
Z_{11}, Z_{12}: 4th-order astigmatism
Z_{13}, Z_{14}: 5th-order coma
Z_{34}: 10th-order spherical aberration

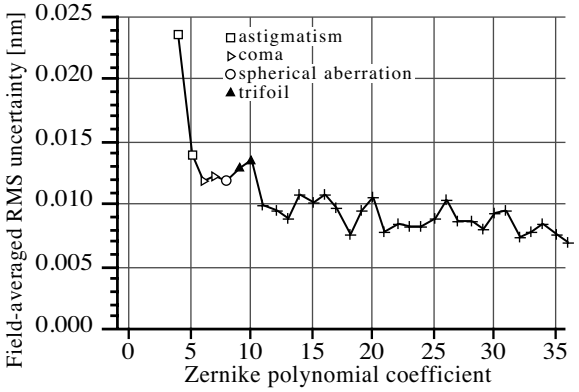

Fig. 5. The average uncertainty in the individual Zernike coefficients of the EUV wavefront measurements performed at all 45 field points. At each point, a number of individual phase-shifted interferograms are recorded. For this calculation, individual wavefronts associated with each exposure are calculated. A fit is performed to determine the aberration polynomial coefficients from each wavefront. When analyzed individually, the variation in the individual fitting coefficients yields the precision of the EUV measurement of each aberration term during this measurement series. Piston, tilt, and defocus terms (coefficients zero through three) are excluded.

The accuracy of the EUV PS/PDI has been studied using an *in situ* null test technique.[3] Within a numerical aperture of 0.088, previous measurements have revealed spherical reference-wavefront accuracy levels of 0.04-nm RMS (λ_{EUV}/330). Because the interferometer uses spatial filtering to produce the reference waves, the accuracy of the PS/PDI generally improves with the quality of the test wavefront being evaluated. Thorough analysis of null-test measurements recorded during the EUV interferometry have not been completed; preliminary analysis suggests an uncalibrated RMS systematic aberration magnitude of approximately λ_{EUV}/200 of 0.065 nm within 0.1 NA. The higher accuracy in prior measurements likely reflects a combination of the smaller NA and a different wavefront error in the optical system under test.

Ultimately, it is through printing that the accuracy and predictive power of the interferometric measurements are verified. The EUV PS/PDI interferometry system has been modified to enable static field imaging experiments with controllable illumination coherence.[13] Imaging experiments conducted on the ETS Set-2 optic are reported in a separate paper in these proceedings (Naulleau, *et al*.). In addition, with the Set-1 optic, the ETS has been used in imaging experiments, and to print targets that are evaluated to measure distortion (see Ref. 14 and Tichenor, *et al*., these proceedings).

3.4 The measurement of low- and high-spatial-frequency aberrations

One unexpected outcome of the interferometry comparison is the fact that the highest spatial frequency aberration terms are those for which the comparison is best. Furthermore, as shown in Fig. 5. the uncertainty in the EUV wavefront measurements is greater for the low-spatial-frequency aberrations than for the higher-spatial-frequency aberrations. It is possible that the variation of low-spatial-frequency aberrations is an inherent challenge associated with point-diffraction class interferometers (visible and EUV) in which the quality of the diffracted wavefront depends on diffraction from a tiny aperture. While interferometers that use point-diffraction may effectively filter the higher-spatial frequency aberrations from the reference wavefront, they may be vulnerable to vibration, small displacements between measure-

ments, and pinhole-shape irregularities. Since it is usually these low-spatial-frequency aberrations that require the highest accuracy in a system alignment process, this issue deserves further study.

4. CONCLUSION

Optics for EUV lithography arguably have the most strict fabrication tolerances of any optical systems fabricated to date, and the development of EUV lithography pushes the advanced optical fabrication techniques toward never before realized levels of figure accuracy and finish quality. As EUV lithography advances toward viability, the need for ultra-high-accuracy wavefront metrology tools has never been greater. Thus far, EUV interferometry performed with the phase-shifting point diffraction interferometer is the most accurate predictor of lithographic performance available for the measurement of EUV optical systems. Only through the inter-comparison of developmental visible-light and other wavefront metrology techniques with an accuracy standard such as the PS/PDI can the commodity of high-accuracy be distributed to the many groups working to create EUV optical systems.

The direct comparison of EUV and visible-light interferometric measurements of the ETS Set-2 optical system represents one part of the effort to identify systematic differences among interferometers and improve the accuracy of all interferometry for EUV applications. Our measurements show that the level of agreement achieved thus far is approximately 0.35 ± 0.11 nm RMS. In an effort to keep the accuracy of interferometry several steps ahead of the quality of the optics under test, this level will have to be improved to well below 0.1 nm (improved perhaps by a factor of 7) in the next several years.

In addition to the wavefront measurements that are presented here, complete characterization of a lithographic optical system requires the measurement of both wavefront quality and distortion. At this time, only the visible-light interferometer has been configured for distortion measurements; the accuracy of which are verifiable only through printing well-calibrated large-field masks, a subject of ongoing research in the ETS.

5. ACKNOWLEDGMENTS

The authors are grateful for the hard work and contributions of the Center for X-Ray Optics engineers and staff including Paul Denham, Keith Jackson, Senajith Rekawa, Kevin Bradley, Brian Hoef, Farhad Salmassi, David Richardson, M. Gideon Jones, Nord Andreson, Drew Kemp, René Delano, Lon Amerman, and David Attwood. We are also indebted to Erik Anderson for electron beam lithography support and development of the pinhole arrays, and to Dino Ciarlo of LLNL for wafer processing. Additional thanks are due for the contributions of LLNL staff in the operation and upgrade of the visible-light interferometer, including Daren Dillon, Nhan Nguyen, Rick Montesanti, Todd Decker, Terry Swan, Carl Chung, Layton Hale, and Gary Otani. This research has been supported by the Extreme Ultraviolet Limited Liability Company (EUV LLC), the DARPA Advanced Lithography Program, and by the Office of Basic Energy Sciences of the U.S. Department of Energy.

6. REFERENCES

1. D. A. Tichenor, G. D. Kubiak, W. C. Replogle, L. E. Klebanoff, J. B. Wronosky, L. C. Hale, H. N. Chapman, J. S. Taylor, J. A. Folta, C. Montcalm, R. M. Hudyma, K. A. Goldberg, and P. Naulleau, "EUV Engineering Test Stand," Proc. SPIE **3997**, 48-69 (2000).

2. H. N. Chapman and D. W. Sweeney, "A rigorous method for compensation selection and alignment of microlithographic optical systems," Proc. SPIE **3331**, 102-113 (1998)

3. P. P. Naulleau, K. A. Goldberg, S. H. Lee, C. Chang, D. Attwood, and J. Bokor, "Extreme-ultraviolet phase-shifting point-diffraction interferometer: a wave-front metrology tool with subangstrom reference-wave accuracy," *Applied Optics* **38** (35), 7252-63 (1999).

4. K. A. Goldberg, P. Naulleau, P. J. Batson, P. Denham, J. Bokor, and H. N. Chapman, "EUV Interferometry of a Four-mirror Ring Field EUV Optical System," Proc. SPIE **3997**, 867-73 (2000).

5. K. A. Goldberg, P. Naulleau, S. H. Lee, C. Chang, C. Bresloff, R. Gaughan, H. N. Chapman, J. Goldsmith, and J. Bokor, "Direct comparison of EUV and visible-light interferometries," Proc. SPIE **3676**, 635-42, (1999).

6. R. Soufli, E. A. Spiller, M. A. Schmidt, C. Davidson, *et al*. "Multilayer optics for an extreme-ultraviolet lithography tool with 70-nm resolution," Proc. SPIE **4343**, 51-9 (2001).

7. G. E. Sommargren, "Phase shifting diffraction interferometer," U.S. Patent **5,548,403**, August, 1996.

8. K. A. Goldberg, P. Naulleau, S. Lee, C. Bresloff, D. Attwood, and J. Bokor, "High-accuracy interferometry of EUV lithographic optical systems," J. Vac. Sci. and Technol. B **16** (6), 3435-3439 (1998).

9. D. T. Attwood, P. Naulleau, K. A. Goldberg, E. Tejnil, C. Chang, *et al*. "Tunable coherent radiation in the soft x-ray and extreme ultraviolet spectral regions," IEEE J. Quant. Elect. **35** (5), 709-20 (1999).

10. P. P. Naulleau, P. J. Batson, P. E. Denham, and M. S. Jones, "Miniature self-contained vacuum compatible electronic imaging microscope," U.S. Patent **6,327,102**, March, 2000.

11. J. S. Loomis, FRINGE User's Manual, (Optical Sciences Center, U. Arizona, Tuscon, AZ, 1976).

12. P. Naulleau, K. A. Goldberg, E. H. Anderson, D. T. Attwood, *et al*. "Static microfield printing at the Advanced Light Source with the ETS Set-2 optic," *these proceedings*.

13. P. Naulleau, K. Goldberg, E. Anderson, P. Batson, P. Denham, S. Rekawa, and J. Bokor, "Adding static printing capabilities to the EUV phase-shifting point diffraction interferometer," Proc. SPIE **4343**, 639-45 (2001).

14. H. N. Chapman, A. K. Ray-Chaudhuri, D. A. Tichenor, W. C. Replogle, *et al*. "First lithographic results from the extreme ultraviolet Engineering Test Stand," J. Vac. Sci. and Technol. B **19** (6), 2389-95 (2001).